Possible TeV Gamma-Ray Binary Origin of HESS J1828–099

Agnibha De Sarkar[1] , Nirupam Roy[2] , Pratik Majumdar[3] , Nayantara Gupta[1] , Andreas Brunthaler[4] , Karl M. Menten[4] ,
Sergio A. Dzib[4] , Sac Nicté X. Medina[4] , and Friedrich Wyrowski[4]

[1] Astronomy & Astrophysics group, Raman Research Institute, C.V. Raman Avenue, 5th Cross Road, Sadashivanagar, Bengaluru 560080, Karnataka, India
agnibha@rri.res.in
[2] Department of Physics, Indian Institute of Science, CV Raman Road, Bengaluru 560012, Karnataka, India
[3] Saha Institute of Nuclear Physics, A CI of Homi Bhabha National Institute, Kolkata 700064, West Bengal, India
[4] Max Planck Institut für Radioastronomie, Auf dem Hügel 69, D-53121 Bonn, Germany
Received 2021 July 19; revised 2022 February 24; accepted 2022 February 25; published 2022 March 17

Abstract

The High Energy Stereoscopic System (H.E.S.S.) observatory has carried out a deep survey of the Galactic plane, in the course of which the existence of a significant number of ($\sim$78) TeV γ-ray sources was confirmed, many of which remain unidentified. HESS J1828–099 is a point-like (Gaussian standard deviation $< 0°.07$) unidentified source among the 17 confirmed point-like sources in the H.E.S.S. Galactic Plane Survey (HGPS) catalog. This source is also unique because it does not seem to have any apparent association with any object detected at other wavelengths. We investigate the nature and association of HESS J1828–099 with multiwavelength observational data. A high-mass X-ray binary (HMXB)—composed of the pulsar XTE J1829–098 and a companion Be star—has been observed earlier in the X-ray and infrared bands, 14′ away from HESS J1828–099. With 12 yr of Fermi-LAT γ-ray data, we explore the possibility of 4FGL J1830.2–1005 being the GeV counterpart of HESS J1828–099. Within the RXTE confidence region, a steep-spectrum ($\alpha_{\mathrm{radio}} = -0.746 \pm 0.284$) plausible counterpart is detected in data from existing radio frequency surveys. In this Letter, we probe for the first time, using multiwavelength data, whether HESS J1828–099, 4FGL J1830.2–1005, and the HMXB system have a common origin. Our study indicates that HESS J1828–099 might be a TeV high-mass γ-ray binary source.

Unified Astronomy Thesaurus concepts: Galactic radio sources (571); Massive stars (732); High mass x-ray binary stars (733); Gamma-ray sources (633); High energy astrophysics (739)

1. Introduction

High-mass γ-ray binaries (HMGBs) belong to a special class of high-mass X-ray binaries (HMXB) that mainly emit in γ-ray energies (Dubus 2013). Such objects comprise compact objects such as a neutron star or a black hole and an O- or Be-type star as the companion. The γ-ray emission in such binaries is usually assumed to be powered by wind-driven shocks (Dubus 2013). The compact object in the HMGBs, usually a rotation-powered pulsar, dissipates its rotational energy by energizing pair plasma, which interacts with wind from the companion star (Maraschi & Treves 1981; Dubus 2006; Huber et al. 2021). In a close-orbit system, a wind collision region is created due to this interaction, which in turn terminates the pulsar and stellar winds by a shock (Bogovalov et al. 2008; Bosch-Ramon et al. 2012; Huber et al. 2021). Particles can be accelerated to ultrarelativistic energies at these shock sites due to diffusive shock acceleration, later producing observed emission through various radiative processes (Sironi & Spitkovsky 2011; Huber et al. 2021). Another favored emission scenario can occur if the massive companion star is a Be star with a disk. In this scenario, the primary interaction happens as the pulsar crosses the circumstellar disk of the Be star, as in the cases of PSR B1259–63 (Aharonian et al. 2005) and PSR J2032+4127 (Lyne et al. 2015). The multiwavelength emission for these two sources differs from other HMGBs, perhaps due to the geometry of the circumstellar decretion disk. For

example, in the case of PSR B1259–63, the light curve in the radio, X-ray, and TeV regimes is typically double peaked and driven by synchrotron (radio and X-ray emissions) and inverse Compton (TeV emission) cooling (Chernyakova et al. 2014). The emission in the GeV range is peculiar given that flares that exceed the pulsar spin-down luminosity have been observed with Fermi-LAT (Abdo et al. 2011; Caliandro et al. 2015; Johnson et al. 2018; Chang et al. 2021). Alternatively, the microquasar model, in which interaction primarily occurs in the jets produced by accretion onto a black hole, also cannot be ruled out (Romero et al. 2003; Bosch-Ramon & Paredes 2004). Only a handful of objects, which have been detected above 100 MeV, are firmly established as HMGBs. Some of the observed HMGBs are HESS J0632–057, 1FGL J1018–5658, PSR B1259–63, LS I+61°303, LS 5039 (Dubus 2015; Li et al. 2017), PSR J2032+4127 (Lyne et al. 2015; Ho et al. 2016; Abeysekara et al. 2018), a point source in the Large Magellanic Cloud (Corbet et al. 2016; H.E.S.S. Collaboration et al. 2018), 4FGL J1405.1–6119 (Corbet et al. 2019), and HESS J1832–093 (Eger et al. 2016; Martí-Devesa & Reimer 2020; Tam et al. 2020). All of these sources have soft spectra in TeV energies and hard, absorbed spectra in X-ray energies.

HESS J1828–099 is a new Very High Energy (VHE) TeV γ-ray source that has been detected in the HGPS (Abdalla et al. 2018a) at the position of R.A. $= 18^{\mathrm{h}}28^{\mathrm{m}}58^{\mathrm{s}}.72$ and decl. $= -09°$ 59′33″.8 (J2000). This H.E.S.S. source is detected at a confidence level of 8.9σ, and the size of the source is $0°.05 \pm 0°.01$, making it 1 of the 17 point-like VHE γ-ray sources found in the HGPS catalog. The flux from this TeV source was recorded for a livetime of 46.3 hr and its 0.20–61.90 TeV spectrum is well fitted by a power law ($\propto E^{-\Gamma_{\mathrm{TeV}}}$) having a photon index of

$\Gamma_{\mathrm{TeV}} = 2.25 \pm 0.12$. Its flux is $1.9\% \pm 0.3\%$ that of the Crab Nebula above 1 TeV and a one-dimensional Gaussian model was used as a spatial template to fit the extent of this VHE source. This H.E.S.S. source is still unidentified as it does not seem to have any apparent association with any other source at lower energies. Earlier, Neronov & Semikoz (2010) claimed that 1FGL J1829.6–1006 (slightly more than $0°25$ away from the H.E.S.S. source) could be the GeV counterpart of the TeV source. They also found that the pulsar J1828–1007 is located $0°1$ from the H. E.S.S. source. Moreover, they claimed the spatial separation between the low- and high-energy emission regions indicate that this source is possibly a pulsar wind nebula (PWN). However, this was not confirmed by the version of the Fermi-LAT catalog available at that time, i.e., the 3FGL catalog (Acero et al. 2015) or the 2FHL catalog (Ackermann et al. 2016). This pulsar is also absent in the latest 4FGL catalog (Abdollahi et al. 2020).

In this Letter, we report our investigations on the origin of the VHE source HESS J1828–099. Analysis of the Fermi-LAT data revealed a possible GeV counterpart, 4FGL J1830.2–1005, spatially coincident with the H.E.S.S. source. A Galactic X-ray source, XTE J1829–098, was also observed by the Chandra X-ray observatory, within the 68% containment radius of 4FGL J1830.2–1005 and $14'$ away from the centroid of HESS J1828–099 (Halpern & Gotthelf 2007), making it a very likely lower-energy counterpart of both the 4FGL and H.E.S.S. sources, based on its position. Pulsar XTE J1829–098 was observed as a transient source by the Rossi X-ray Timing Explorer (RXTE) observatory during the scan of the Galactic plane in 2003 July–August (Markwardt et al. 2004). The best-fit pulsar position was found to be R.A. $= 18^{\mathrm{h}}29^{\mathrm{m}}35^{\mathrm{s}}$ and decl. $= -09°51'0''00$ (J2000), with a 99% confidence region of approximately elliptical shape, with semimajor axes of $3''8$ (RA) and $3'$ (decl.) (Markwardt et al. 2004). Subsequent X-ray Multi-Mirror Mission (XMM-Newton) observations found the position of this source to be R.A. $= 18^{\mathrm{h}}29^{\mathrm{m}}44^{\mathrm{s}}1$ and decl. $= -09°51'24''1$ (J2000), with a 90% uncertainty radius of $3''2$ (Halpern & Gotthelf 2007). It was discovered in the RXTE data that this pulsar has a rotation period of ~ 7.8 s (Markwardt et al. 2004), which was later confirmed by various other observations (Halpern & Gotthelf 2007; Shtykovsky et al. 2018). Analyzing XMM-Newton data, a hard power-law photon index, Γ_X^{XMM}, of 0.76 ± 0.13, and a hydrogen column density N_H, of $(6.0 \pm 0.6) \times 10^{22}$ cm^{-2} were estimated in the soft X-ray range (2–10 keV), both given with their 1σ uncertainties (Halpern & Gotthelf 2007). This suggests that this pulsar is part of an HMXB, as the best-fit value of N_H exceeds the measured Galactic 21 cm H I column density, in the pulsar's direction, of $\sim 1.81 \times 10^{22}$ cm^{-2} (Dickey & Lockman 1990), $\sim 1.43 \times 10^{22}$ cm^{-2} (Leiden/Argentine/Bonn (LAB) survey; Kalberla et al. 2005), and $\sim 1.79 \times 10^{22}$ cm^{-2} (HI4PI survey; Ben Bekhti et al. 2016), indicating that some absorption is intrinsic to the binary, either from the wind or circumstellar disk of the companion star. A candidate source, $2''1$ away from XMM-Newton location of XTE pulsar, was detected in the analysis of the data obtained by Chandra (Halpern & Gotthelf 2007). The Chandra location of this source was found to be R.A. $= 18^{\mathrm{h}}29^{\mathrm{m}}43^{\mathrm{s}}97$ and decl. $= -09°51'23''2$ (J2000), with a 90% positional uncertainty of $0''6$. Assuming the same best-fit XMM-Newton parameters, the average flux of the source, detected by Chandra in the soft X-ray range, was found to be consistent with that from the XMM-Newton observations (Halpern & Gotthelf 2007). A

hard, absorbed spectrum estimated from the analysis of archival data obtained by the Swift X-ray Telescope (XRT) ($\Gamma_X^{\mathrm{Swift}} = 1.1_{-0.8}^{+0.9}$, $N_H = 10_{-4}^{+6} \times 10^{22}$ cm^{-2}) reinforces this source's identification as an HMXB (Sguera et al. 2019). This source has shown frequent outbursts over the years, observed by different observatories. The MAXI gas slit camera (GSC) detected four outbursts from this source in 11 yr of observation, including one on 2021 April 12 (Nakajima et al. 2021). The time intervals between these outbursts match the proposed orbital period (≈ 246 days) of the binary system (Markwardt et al. 2004; Nakajima et al. 2021). Sguera et al. (2019) had checked 15–50 keV XTE source light curve on a daily timescale from the Swift Burst Alert Telescope archive and found that the duration of the outburst was very likely of the order of 3–4 days, which is almost the same order of duration estimated by Markwardt et al. (2009) (~ 7 days). In 2018 August, an X-ray outburst from this source triggered a ToO observation with the Nuclear Spectroscopic Telescope Array (NuSTAR), which showed the existence of a cyclotron absorption line at $E_{\mathrm{cyc}} = 15.05 \pm 0.06$ keV, implying that the magnetic field on the neutron star surface is $B \simeq 1.7 \times 10^{12}$ Gauss (Shtykovsky et al. 2018). The detection of the cyclotron absorption line in the X-ray spectrum of the pulsar confirmed that this pulsar is part of an HMXB.

A star was found in infrared (IR) analysis within $0''2$ of the Chandra localization of XTE J1829–098 (Halpern & Gotthelf 2007). This bright, infrared counterpart was detected in the Two Micron All Sky Survey (2MASS), but it is not visible in the optical range. The measured IR magnitudes of this companion star are $K = 12.7$, $H = 13.9$, $I > 21.9$, and $R > 23.2$ (Halpern & Gotthelf 2007). From the measured magnitude in the H and K bands, the distance of this companion was estimated to be approximately 10 kpc. Assuming this distance, the maximum observed X-ray luminosity in the 2–10 keV range was found to be 2×10^{36} erg s^{-1} and minimum luminosity as 3×10^{32} erg s^{-1}, similar to a wind-driven system or a Be binary transient (Halpern & Gotthelf 2007). Later observations by Sguera et al. (2019) found that the reddening-free near-infrared (NIR) diagnostic color criterion Q has a value of -0.7, which is very typical of an early-type OB star, although it can also be a Be star. According to the Corbet diagram (Corbet 1984, 1985, 1986), for a possible orbital period of ≈ 246 days, there is a greater likelihood that the donor star is a Be star. Moreover, the absence of a Hα emission line in the NIR spectra of the 2MASS counterpart is indicative of the NIR counterpart being a Be star.

Data analysis and the corresponding results are discussed in Section 2. In Section 2.1, we present the results of the analysis of NuSTAR data and report the detection of a subdominant, intrabinary shock emission component. Based on this detection and spatial association, we suggest that this HMXB has a common origin with both of the 4FGL and H.E.S.S. sources. In Section 2.2, we present the results of the analysis of ~ 12 yr of Fermi-LAT data. We have also used multiwavelength radio continuum data to identify any radio counterpart of the H.E.S.S. source. In Section 2.3, we discuss the detection of a nearby source in multi-radio-frequency surveys and investigate this as the likely radio counterpart of the H.E.S.S. source based on its position. In Section 3, we present the results of one-zone leptonic modeling to fit the multiwavelength spectral energy distribution (SED) and show that the required values of the parameters are consistent with those of other established

HMGBs (Hinton et al. 2009). Finally, in Section 4, we discuss the results and the caveats of our model. We also suggest the additional observations that are required to completely explain the multiwavelength SED of the system. Finally, we conclude that HESS J1828–099 is possibly a TeV HMGB, based on spatial coincidence and spectral properties.

2. Data Analysis and Results

2.1. X-Ray Data Analysis

Although XTE J1829–098 was confirmed to be an HMXB, the presence of an iron Kα emission line, the cyclotron absorption line, and the exponential cutoff, as reported in Shtykovsky et al. (2018), point toward the fact that the pulsar is accreting and the dominant X-ray flux seen from this source is due to the accretion. However, in previous analyses of established TeV HMGBs (Takahashi et al. 2009; An et al. 2015; Volkov et al. 2021), no spectral lines and/or cutoff or spectral turnover at higher energies were found, indicating, as in general for TeV HMGBs, that the pulsar usually is not accreting. Also, the best-fit cutoff power-law spectral index obtained from NuSTAR data analysis is notably different compared to what is predicted if we assume that the observed X-rays represent synchrotron emission. These factors put the TeV HMGB interpretation of HESS J1828–099 to the question.

To resolve this discrepancy, we tried to find whether or not the pulsar in this case is actively accreting by comparing the Alfvén radius (R_{Alf}) with the corotation radius (R_{co}). If $R_{Alf} < R_{co}$, then material from the companion star accretes on the pulsar surface; if $R_{Alf} \gg R_{co}$, then the stellar material directly interacts with pulsar's rotating magnetosphere and subsequently gets ejected, known as the propeller phase. Finally, if $R_{Alf} \simeq R_{co}$, then these two effects happen simultaneously and intermittent accretion occurs, which is the intermediate stage between the accretor and propeller phases.

The corotation radius (R_{co}) is defined as the radius at which the spin angular velocity ($\Omega_s = 2\pi/P_s$) of the pulsar is equal to the Keplerian angular velocity ($\Omega_k = \sqrt{GM_*/r^3}$) of the material being accreted. Assuming a standard pulsar mass of $1.5M_\odot$ and using the observed XTE J1829–098 rotation period (P_s) of 7.8 s, we get

$$R_{co} = \left(\frac{GM_*}{4\pi^2} \times P_s^2\right)^{\frac{1}{3}} \simeq 6 \times 10^8 \text{ cm.} \qquad (1)$$

The Alfvén radius (R_{Alf}) is defined as the radius where the ram pressure of the infalling material from the companion star (ρv^2) balances the magnetic pressure of the pulsar magnetosphere ($B^2/8\pi$). Assuming typical values for a pulsar, mass of $1.5M_\odot$, and radius $R_* = 10^6$ cm, the observed magnetic field of $B \simeq 1.7 \times 10^{12}$ G, resulting in a magnetic moment, μ, of $B R_*^3 \simeq 1.7 \times 10^{30}$ G cm^3 and observed X-ray luminosity $L_X \simeq 4.3 \times 10^{36}$ erg s^{-1} (Shtykovsky et al. 2018), we get the Alfvén radius as (Lamb et al. 1973; Becker et al. 2012)

$$R_{Alf} = 2.6 \times 10^8 \left(\frac{\Lambda}{1}\right)\left(\frac{M_*}{M_\odot}\right)^{\frac{1}{7}}\left(\frac{R_*}{10^6 \text{ cm}}\right)^{-\frac{2}{7}}$$
$$\times \left(\frac{L_X}{10^{37} \text{ erg s}^{-1}}\right)^{-\frac{2}{7}}\left(\frac{\mu}{10^{30} \text{ G cm}^3}\right)^{\frac{4}{7}} \text{cm} \simeq 5 \times 10^8 \text{ cm,} \qquad (2)$$

where the constant Λ signifies the geometry of the accretion flow. Following Becker et al. (2012), there is an uncertainty on the value of Λ, which is $\Lambda = 1$ for spherical accretion and $\Lambda < 1$ for disk accretion. Because very distinct accretion disks usually do not form in the case of HMXBs (Reig 2011; Karino et al. 2019), in this Letter, we assume a wind-fed spherical accretion ($\Lambda = 1$) for simplicity. R_{Alf} for spherical accretion as given in Equation (2), is very close to R_{co}, making this a case for intermittent accretion. In this regime, a turbulent and magnetized transition zone can be formed close to R_{Alf}, due to the balance between the magnetic pressure and the pressure inserted by accreting matter. Part of the infalling matter accumulated at the transition zone can further accrete onto the pulsar surface (accretor phase). However, the rotating pulsar magnetosphere can also strongly shock the infalling material at the transition region, ejecting some of it beyond the accretion radius (propeller phase). Electrons can get shock-accelerated to very high energies at this transition region and can further produce X-rays via the synchrotron mechanism (Lovelace et al. 2005; Bednarek 2009; Torres et al. 2012; Romanova & Owocki 2015). Although X-rays produced from accretion are the dominant component observed during the outburst phase, a subdominant X-ray component at higher energies, produced from shocked electrons, should also be present in the data observed by NuSTAR during the same outburst phase.

To confirm this observationally, we have analyzed the data obtained by NuSTAR on 2018 August 16 (ObsID 90401332002), with an on-source exposure time of ∼27.8 ks and an average count rate of ∼8 cts s^{-1} per module (Shtykovsky et al. 2018). To extract the spectra, we have used the NuSTAR-DAS 2.0.0 software as distributed with the HEASOFT 6.28 package, with CALDB version 20210315. The source data were extracted from a circular region of radius 50″, centered on the source position. The background data were extracted similarly from a circular region of radius 70″, away from the source position. The NuSTAR observations are not affected by stray light. The obtained spectra were grouped to have 25 counts per bin using the grppha tool. The spectral analysis was done using the XSPEC 12.11.1 tool included in the HEASOFT 6.28 package. As the background starts to dominate the source counts above 50 keV, in this Letter, we have considered the 3–45 keV energy range for spectral analysis.

According to Shtykovsky et al. (2018), the spectrum of XTE J1829–098 can be explained by a power law with an exponential cutoff (cutoffpl model), modified by the fluorescent iron emission line (Gaussian line profile model Gauss) and an absorption line (Gaussian absorption line model gabs), which is interpreted as a cyclotron resonant scattering feature (CRSF). So we have analyzed the phase-averaged NuSTAR data and tried to fit the spectrum with the model constant*tbabs*(cutoffpl*gabs + Gauss), representing the accretion component. We have used the tbabs model to take into account the X-ray absorption by the interstellar medium (ISM). To keep the best-fit values of the model consistent with the best-fit results obtained by Shtykovsky et al. (2018), we have kept the value of the hydrogen column density N_H in the direction of XTE J1829–098 fixed at 1.43×10^{22} cm^{-2} (LAB survey; Kalberla et al. 2005). We have used atomic cross sections from

Table 1
Upper Panel: Best-fit Parameters of the Model
constant*tbabs*(cutoffpl*gabs + Gauss), along with their 1σ
Uncertainties. Lower Panel: Best-fit Photon Spectral Index of the Additional
Power-law Component, along with Its 1σ Uncertainty

Parameter	Value
Hydrogen column density, N_H (cm^{-2})	1.43×10^{22}
Photon index of the cutoff power law, $\Gamma_X^{\text{cutoffpl}}$	$-0.75^{+0.03}_{-0.03}$
Folding energy of exponential roll-off, E_{fold} (keV)	$4.49^{+0.06}_{-0.06}$
Cyclotron line energy, E_{cyc} (keV)	$15.20^{+0.10}_{-0.10}$
Cyclotron line width, W_{cyc} (keV)	$2.37^{+0.10}_{-0.10}$
Optical depth at cyclotron line center, τ_{cyc}	$0.55^{+0.05}_{-0.05}$
Fe Kα line energy, E_{Fe} (keV)	$6.52^{+0.04}_{-0.04}$
Fe Kα line width, σ_{Fe} (keV)	$0.22^{+0.04}_{-0.04}$
Photon index of the power law, Γ_X^{pl}	$1.50^{+0.15}_{-0.10}$

Verner et al. (1996) and elemental abundances from Wilms et al. (2000). The best-fit values, along with their 1σ uncertainties (χ^2/D.O.F. $= 1196.19/1071 \approx 1.12$), are shown in the upper panel of Table 1. Considering the uncertainties, the measured values of the model are consistent with those given in Shtykovsky et al. (2018). The flux obtained from the model in the 3–79 keV energy range was found to be $F_X^{\text{acc}} \simeq (3.66 \pm 0.02) \times 10^{-10}$ erg cm^{-2} s^{-1}. The spectrum fit, along with residual and data/model ratio, is shown in Figure 1(a). Although the best-fit values give a very good fit at low and intermediate energies, the best-fit model deviates from the data at higher energies, which is evident from the residual and ratio plots. This discrepancy hints toward a second emission component from the same source region.

Next, we have added an additional power-law spectrum, in the form of the model pow, with the above model signifying accretion, to fit the data. We have let the parameters of the power-law component freely vary while keeping the best-fit values given in the upper panel of Table 1 fixed. The best-fit photon spectral index value of the additional power law is given in the lower panel of Table 1. As found in other established HMGBs, the spectral index of the power law can vary between 1.4 and 1.6 (Takahashi et al. 2009). It can be readily seen that the best-fit value along with the uncertainty of the additional power-law component spectral index agrees well with previous observations. The obtained data and the corresponding best-fit model, along with the residual and the ratio, after fitting the data with the model constant*tbabs*(cutoffpl*gabs + Gauss + pow), are shown in Figure 1(b). From the figure, it can be seen that the data are fitted comparatively well at higher energies after the addition of the power-law model (χ^2/D.O.F. $= 1187.15/1076 \approx 1.10$). The absorbed flux of the subdominant power-law component in the energy range of 3–79 keV was found to be $F_X^{\text{pl}} \simeq (9.6 \pm 0.8) \times 10^{-12}$ erg cm^{-2} s^{-1}, and the corresponding luminosity is $L_X^{\text{pl}} \simeq (1.1 \pm 0.1) \times 10^{35}$ (d/10 kpc)^2 erg s^{-1}.

It was found that the improvement in the χ^2 statistic after the addition of the subdominant power-law component with the accretion component is small. We have also calculated the F-statistic probability using ftest tool present in XSPEC. We have used appropriate χ^2 and D.O.F. values for the calculation and found that the F-statistic probability ($\approx 1 \times 10^{-2}$), although $\ll 1$, is comparatively high. These results suggest that the addition of the subdominant power-law component with the accretion component is, although reasonable, of low statistical

significance. This is not surprising as the additional power-law component is subdominant compared to the dominant accretion component in the outburst phase of the XTE source. Moreover, the marginal improvement in the fit statistics can be attributed to the low number of data points available to constrain the additional power-law component in the hard X-ray range. Nevertheless, the improvement in the residual and the ratio associated with the data and model X-ray spectrum (see Figures 1(a) and (b)), justify the addition of the subdominant power-law component. Observational detection of this power-law component, in conjunction with the argument presented above in terms of different characteristic radii, suggests that X-rays produced from shocked electrons through synchrotron cooling are also present in the source region. In Appendix A, we present the significance of the subdominant power-law component, obtained using the Monte Carlo simulation method. We note that calculating R_{Alf} with $\Lambda = 0.5$, as what may be expected from disk-fed accretion, yields an Alfvén radius of $R_{\text{Alf}} \simeq 2 \times 10^8$ cm, which is, although of the same order, somewhat less than R_{co}. This may imply that the infalling material from the companion star accretes on the pulsar surface, without being propelled at the transition region. Consequently, no shock is created at the transition region in case of disk-fed accretion. However, the signature of the shock component is observed in the NuSTAR data, represented by the subdominant power-law component, indicating that our assumption of a wind-fed spherical accretion is valid. The presence of the subdominant, nonthermal power-law emission indicates that this source indeed shows typical characteristics of an HMGB (Takahashi et al. 2009; An et al. 2015; Volkov et al. 2021). We have also performed pulse phase-resolved spectroscopy of the observed NuSTAR data in four different phase bins of equal sizes, spanning the entire phase range of 0–1, using the same model described above. But due to relatively low source photon counts, as well as large uncertainties associated with the data points, the phase dependence of the subdominant power-law component could not be unambiguously established. Multiple simultaneous X-ray observations can help elucidate the phase dependence of the shock component.

2.2. GeV Counterpart of HESS J1828–099

Despite being very prominent in TeV energies, HESS J1828–099 has not been properly identified in GeV energies. For a deeper search of its GeV counterpart, we have analyzed ∼12 yr of Fermi-LAT data, observed between 2008 August 4 (MJD 54682) and 2020 October 2 (MJD 59124) in the 0.3–500 GeV band. A full description of the GeV data analysis is presented in Appendix B. The closest GeV source is 4FGL J1830.2–1005, which was detected at a best-fit position of R.A. $= 277^\circ.5300 \pm 0^\circ.0342$, and decl. $= -10^\circ.0730 \pm 0^\circ.0262$, only $0^\circ.292$ away from the centroid of the H.E.S.S. source. 4FGL J1830.2–1005 was detected with a test statistic (TS) value of 458.53 and its spectral shape is log-parabolic, expressed by the form

$$\frac{dN}{dE} = N_0 \left(\frac{E}{E_b}\right)^{-\left(\alpha_{\text{GeV}} + \beta_{\text{GeV}} \log\left(\frac{E}{E_b}\right)\right)}. \qquad (3)$$

The best-fit parameters are $\alpha_{\text{GeV}} = 3.491 \pm 0.011$, $\beta_{\text{GeV}} = 0.7651 \pm 0.0059$, and $E_b = 1.396$ GeV. The average energy flux of this source is $F_\gamma^{\text{GeV}} = (1.88 \pm 0.02) \times 10^{-5}$ MeV cm^{-2} s^{-1}. This flux is included in the SED shown in Figure 3.
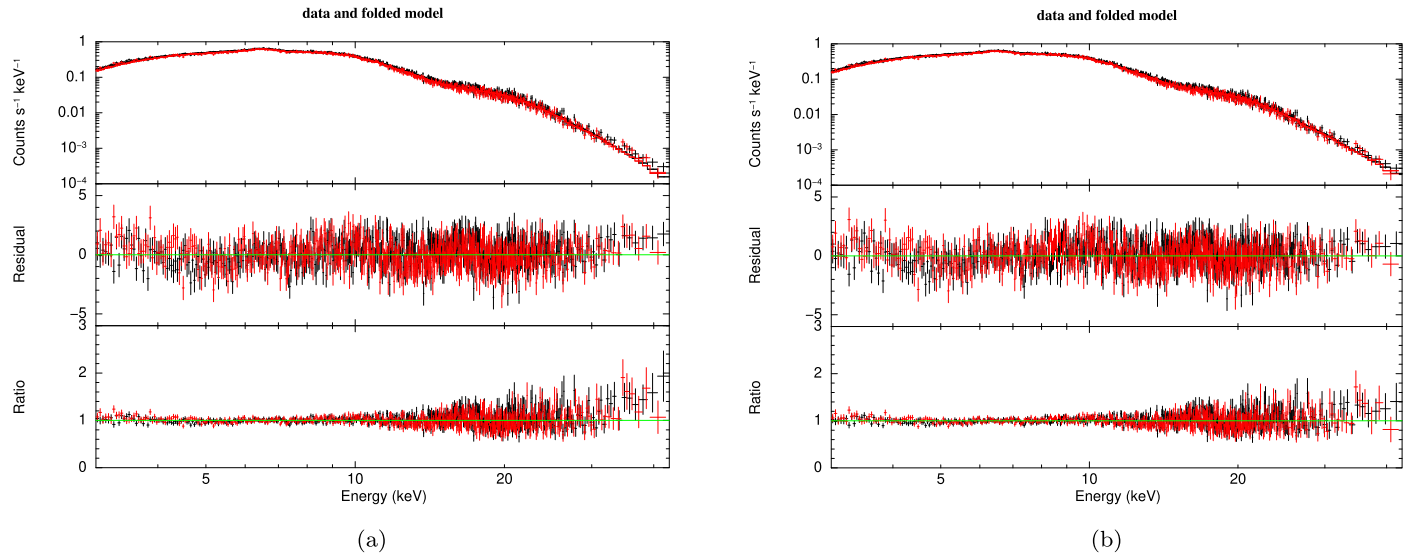
Figure 1. (a) Data and model spectrum fit, the residual, and the ratio (data/model) for the best-fit values given in the upper panel of Table 1. The model used in this case is `constant*tbabs*(cutoffpl*gabs + Gauss)`. FPMA and FPMB data points and best fits are shown in black and red, respectively. (b) Data and model spectrum fit, the residual, and the ratio (data/model), after addition of a power-law component with the best-fit model used in (a). Model used in this case is `constant*tbabs*(cutoffpl*gabs + Gauss + pow)`. The color scheme is the same as in (a).

We have analyzed the extension of the 4FGL J1830.2–1005 using the RadialDisk and RadialGaussian models as templates. Fitting the extension with the RadialDisk template gives a maximum TS_{ext} value of 32.41 ($\sim 5.692\sigma$), with the best-fit 68% containment radius of the disk being $0°\!.325 \pm 0°\!.037$. We have considered radial disks of radius varying from $0°$ to $0°\!.5$ to show how the delta log-likelihood varies with increasing radius (see Figure 2(b)). We have also studied the energy-dependent morphology of the source by estimating the extent in two different energy ranges, 0.3–1 GeV and 1–500 GeV. We found that the spatial extent in both cases remains almost the same, $0.3063^{+0.0630}_{-0.0692}$ deg in the 0.3–1 GeV range and $0.2875^{+0.0517}_{-0.0463}$ deg in the 1–500 GeV range. It was found that the offset in the spatial position of the 4FGL source at different energy ranges varies significantly from the original 4FGL source position (offset $\approx 0°\!.1068$ in the energy range 1–500 GeV and offset $\approx 0°\!.0198$ in the energy range 0.3–1 GeV). The energy-dependent morphology of the sources is shown in Figure 2(a). From the figure, it can be seen that the 4FGL source and the H.E.S.S. source overlap with each other. Also, with increasing energy (in the 1–500 GeV range), we observe an increment in spatial proximity between the 4FGL and the H.E.S.S. sources. Based on the positional coincidence between these two sources, it can be inferred that 4FGL J1830.2–1005 can possibly be the GeV counterpart of HESS J1828–099. A periodicity search was carried out to probe any possible periodic variation in the GeV γ-rays from the 4FGL source, but no significant periodicity was found. Details of the periodicity search are presented in Appendix C.

2.3. Radio Counterpart of HESS J1828–099

We have used multiwavelength radio data from different surveys to look for possible counterparts of HESS J1828–099. The field is observed as a part of the recent high-sensitivity Galactic plane surveys like the THOR survey (the H I/OH/ Recombination line survey; Beuther et al. 2016; Wang et al. 2020) covering 1–2 GHz and the GLOSTAR Galactic Plane survey (A GLObal view of STAR formation Brunthaler et al. 2021) covering 4–8 GHz. Due to the proximity of the

source to the Galactic plane, the field is crowded with multiple resolved and unresolved sources including Galactic (H II regions, supernova remnants, planetary nebulae) as well as many unclassified Galactic as well as extragalactic sources (Chakraborty et al. 2020). Near the position of XTE J1829–098, we detect a radio source within the 99% RXTE confidence region in both THOR and GLOSTAR images and investigate this as a plausible radio counterpart of the HMXB based on its proximity. A full description of the radio data analysis is presented in Appendix D.

Figure 2(c) shows the 1.4 GHz THOR+VGPS image of the field at $25''$ resolution. There is no radio emission at the Chandra position of XTE J1829–098. However, within the RXTE error region, marked by the ellipse with a crosshair at the center, there is a prominent radio source detected in THOR. The source is marginally resolved, and the L-band peak flux density of this source at an effective frequency of 1.63 GHz is 4.15 ± 0.25 mJy beam^{-1}.

The source identified from THOR as the possible counterpart of the binary system, marked by a small white circle in Figure 2(c), is also detected in the GLOSTAR survey and has a peak flux density of 2.30 ± 0.21 mJy beam^{-1} (Figure 2(d)). The flux density values from the GLOSTAR subimages are consistent with the in-band spectral index (α_{radio} where $S_\nu \propto \nu^{\alpha_{radio}}$) of -0.746 ± 0.284 estimated from the flux values in different THOR spectral windows (SPWs). The observed radio spectrum is indicative of particle acceleration due to the collision of an ultrarelativistic pulsar wind and the wind/disk of the normal star. The extended nature of the source indicates its possible Galactic origin. In the complete catalog of the D-configuration continuum sources (S. N. X. Medina et al. 2022, in preparation), it is classified as a candidate planetary nebula based on its mid-IR properties. However, the nondetection of this source in the earlier 1.4 GHz NVSS image (the NRAO VLA Sky Survey; Condon et al. 1998) at $45''$ resolution also indicates the variability of this source. We note that the putative radio source is also detected at 147.5 MHz in the TIFR GMRT Sky Survey (TGSS; Intema et al. 2017) with a flux density of 51.14 ± 8.45 mJy. The SED in Figure 3 includes the multiwavelength radio data from the TGSS, THOR SPWs, as well as from GLOSTAR

(a)

(b)

(c)

(d)
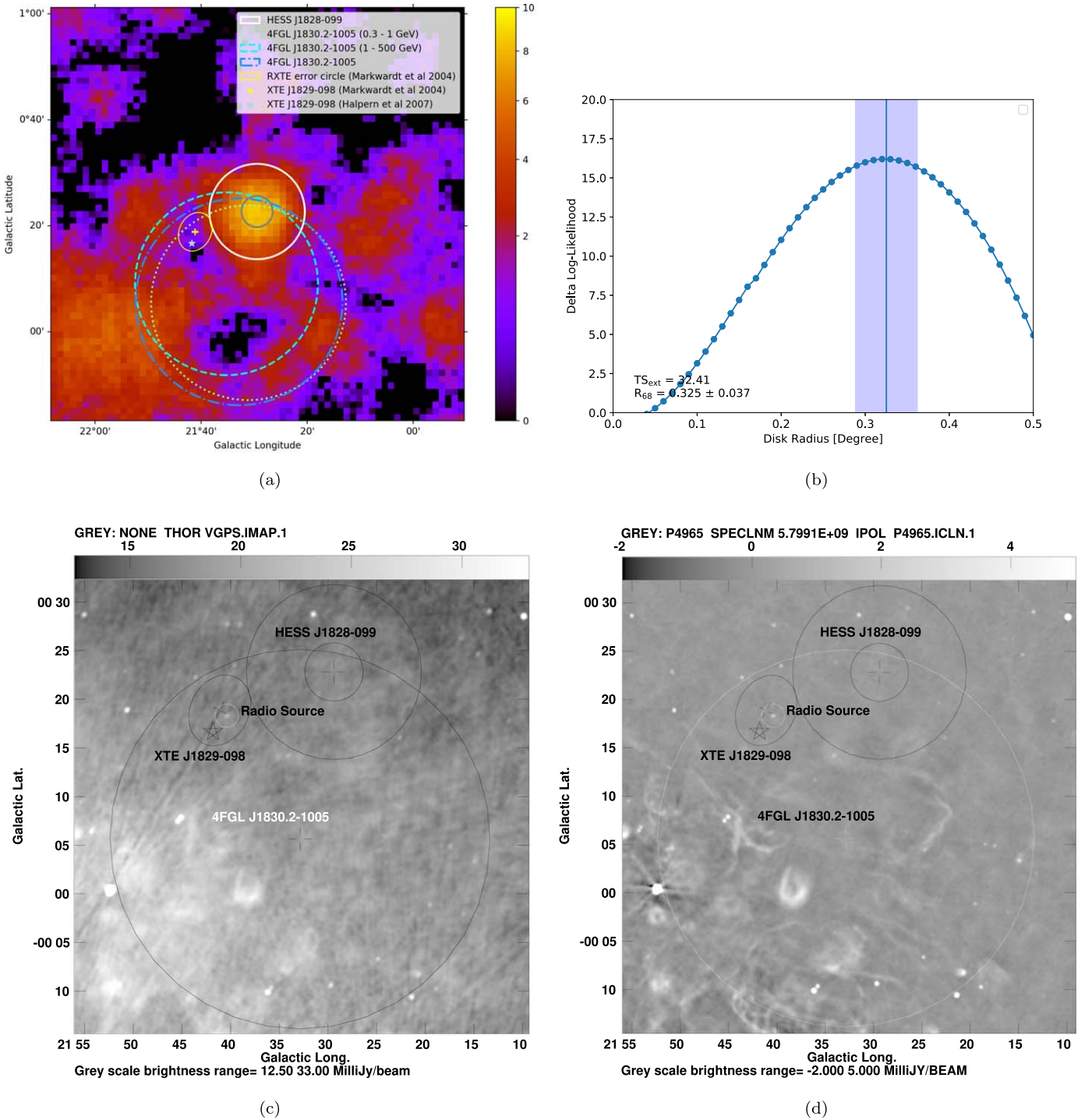
Figure 2. (a) H.E.S.S. significance map centered on HESS J1828–099. The color bar denotes the $\sqrt{\mathrm{TS}}$ value of the region. The gray circle represents the extent to which a 1D Gaussian template was fitted, and the white circle signifies the region within which spectral points for HESS J1828–099 were extracted. Morphologies of 4FGL J1830.2–1005 at different energy ranges are shown with the green dotted line (0.3–1 GeV) and the cyan dashed line (1–500 GeV). Blue dotted–dashed line signifies a spatial extension of the 4FGL in the entire considered energy range (0.3–500 GeV). The RXTE position of pulsar XTE J1829–098 (Halpern & Gotthelf 2007), along with the 99% confidence region (Markwardt et al. 2004), is also shown in yellow. The Chandra position of the pulsar is shown with a light-blue star. (b) Variation of the delta log-likelihood value of 4FGL J1830.2–1005 modeled with radial disks of different radii. The blue shaded region indicates the uncertainty estimate of the best-fit extension of 4FGL J1830.2–1005. (c) The combined THOR and VGPS 1.4 GHz image and (d) the GLOSTAR 5.8 GHz image showing the radio continuum emission from the field containing HESS J1828–099, 4FGL J1830.2–1005, and the pulsar XTE J1829–098. The Chandra position of the pulsar is marked with a star, and the RXTE error region is shown with a black ellipse. Spatial extent marked for the H.E.S.S. and the 4FGL sources (0.3–500 GeV) is the same as in (a). Plausible radio counterpart of the binary system is marked by a white circle.

subimages. Considering the spectral index, possible variability, and the position of the source (within the RXTE error region but not coinciding with the Chandra position of XTE J1829–098), in the subsequent analysis, we consider both the possibilities that this

radio source may or may not be a counterpart of HESS J1828–099. For the scenario where it is not associated, we have used the 3σ limits from the GLOSTAR, THOR, and TGSS to construct (and model) the SED.

(a)

(b)

(c)

(d)

(e)

(f)
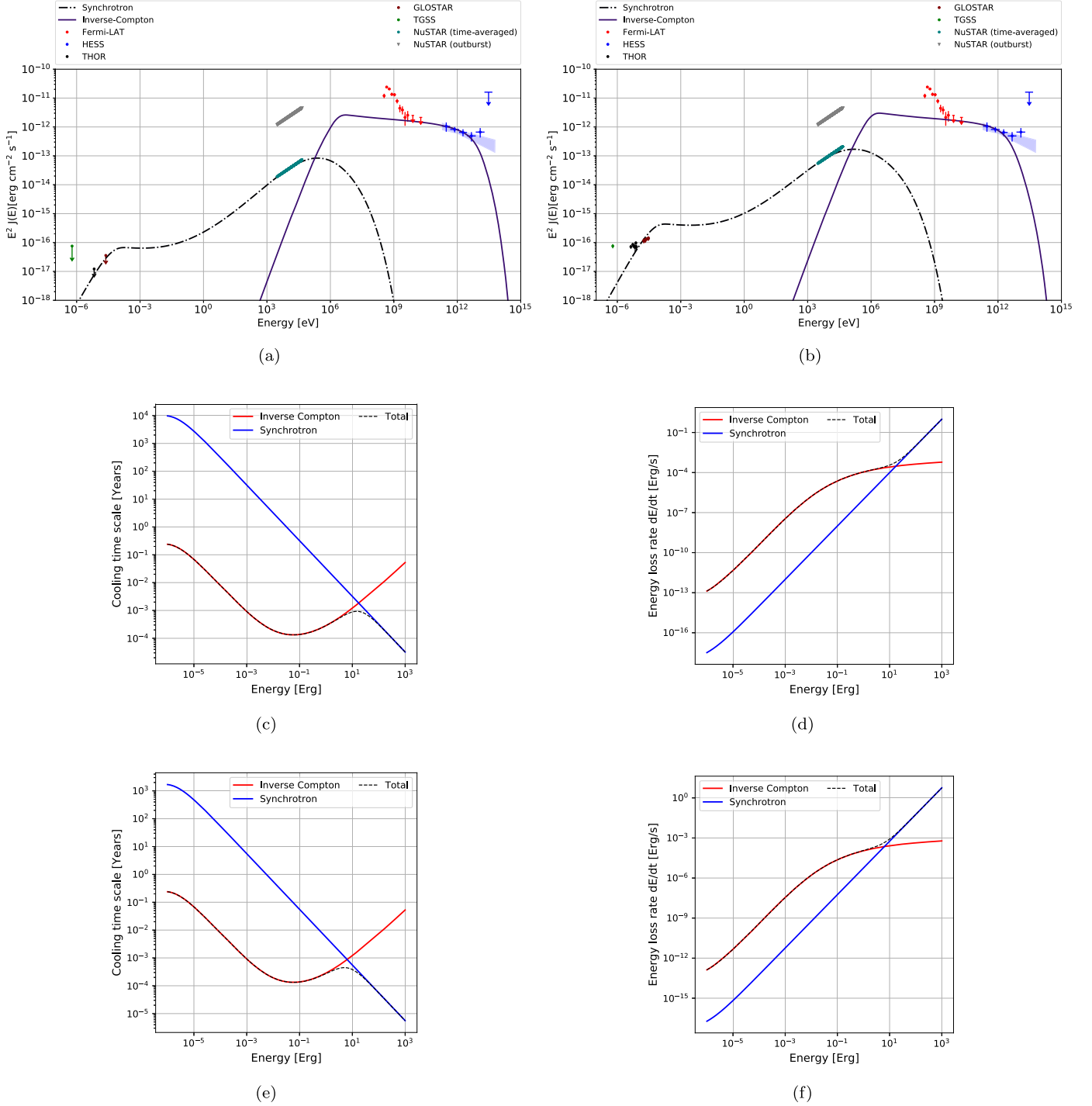
Figure 3. Multiwavelength SED of the source HESS J1828–099 and corresponding IC dominated (a) model 1 and (b) model 2, obtained using GAMERA. The unabsorbed power-law X-ray SED obtained from NuSTAR data analysis in the outburst phase of XTE J1829–098 is shown with gray data points. The same unabsorbed X-ray SED, time-averaged over the orbital period of XTE J1829–098 (Halpern & Gotthelf 2007) is shown with teal data points. The H.E.S.S. data, shown in blue, were taken from Abdalla et al. (2018a). We have analyzed the Fermi-LAT data and the corresponding SED from 4FGL J1830.2–1005 is shown in red. The 3σ upper limits at radio range, obtained at the Chandra position of XTE J1829–098, observed by THOR (black), GLOSTAR (maroon), and TGSS (green), are shown in (a) with downward arrows. In (b), flux values of the putative radio source from these surveys are shown with the same color scheme. In (c) and (d), we present the cooling timescale and energy-loss rate of model 1, at time $t = t_{age} \approx 10^7$ yr. In (e) and (f), we plot the same as (c) and (d), for model 2.

3. Multiwavelength SED Modelling

We have accumulated the data obtained from different multiwavelength observations, shown in Figures 3(a) and (b), to perform multiwavelength SED modeling. We have considered a leptonic, Inverse Compton (IC)-dominated, one-zone model, similar to Hinton et al. (2009) to explain the emission

from HESS J1828–099. Because there is an offset between the Chandra position of XTE J1829–098 and the putative radio source found in the RXTE error region, we have explored two different cases to explain the multiwavelength SEDs. In Model 1, we consider 3σ upper limits for radio flux density at the exact Chandra position of XTE J1829–098 and use these upper

Table 2
Parameters Used for the Two Models

Model	$E_{\min}$ (GeV)	$E_{\max}$ (GeV)	α_e	B (mG)	T_* (K)	U_{rad} (erg cm^{-3})	Age (Years)	Distance (kpc)
Model 1	0.12	5×10^4	2.2	25	30,000	1	10^7	10
Model 2	0.08	5×10^4	2.2	60	30,000	1	10^7	10

limits to construct the SED at radio frequencies, whereas in Model 2, the radio source within the RXTE error region is assumed to be the radio counterpart of the HMXB and the GLOSTAR/THOR/TGSS data are used to extend the SED to radio wavelengths.

The HMXB XTE J1829–098 is located at a distance of 10 kpc from Earth (Halpern & Gotthelf 2007). Because the companion star of the HMXB probably is a Be star, we assume its age is $t_{\mathrm{age}} \leqslant 10^7$ yr and the stellar photon temperature T_* is $\approx$30,000 K (Takata et al. 2017). We have considered a population of accelerated electrons having a cutoff power-law spectrum, $dN/dE_e \propto E_e^{-\alpha_e} \exp(-E_e/E_{\max})$ in the shock region between the pulsar and the companion star. The small distance between the companion star and the pulsar ($\sim$0″.2) indicates that a photon field with high radiation density is present in the region. Ultrarelativistic electrons are cooling down by synchrotron and IC emission. Radio to X-ray emission is produced due to synchrotron emission and γ-rays are produced by IC emission. As discussed in Section 2.1, we detected a subdominant power-law X-ray component with a spectral index of $1.50^{+0.15}_{-0.10}$, which implies that the energy spectrum of parent electrons should have a power-law spectral index $\alpha_e = 2\Gamma_X^{\mathrm{pl}} - 1 = 2.0^{+0.3}_{-0.2}$. We have searched within this range to find the best-fit spectral index for the parent electron spectrum for both model 1 and model 2. Moreover, we have also used an exponential cutoff in the parent electron spectrum because electrons, being leptons, lose energy very efficiently. We have assumed $E_{\max} = 50$ TeV, maximum energy up to which the parent electrons can be accelerated in the shock site.

By analyzing the NuSTAR data, the fluxes of the accretion component ($F_X^{\mathrm{acc}} \simeq (3.66 \pm 0.02) \times 10^{-10}$ erg cm^{-2} s^{-1}) and the shock component ($F_X^{\mathrm{pl}} \simeq (9.6 \pm 0.8) \times 10^{-12}$ erg cm^{-2} s^{-1}) in the 3–79 keV range, during the outburst phase, were determined, as discussed in Section 2.1. But XTE J1829–098, being a transient source, shows a very high observed dynamic range ($\sim$6800) (Halpern & Gotthelf 2007), which indicates that the value of F_X^{acc} can decrease down to $\sim$10^{-14} erg cm^{-2} s^{-1} in its most quiescent phase. The flux of the shock component F_X^{pl} will also decrease when the XTE source is not in the outburst phase. Due to the lack of long-term observational data, we assume that the time-averaged flux of the shock component over the entire orbital periodic revolution is $(1-5) \times 10^{-2}$ times the flux measured in the outburst phase. This assumption is not unreasonable because the XTE source spends comparatively less time in the outburst phase during its orbital motion, making the time-averaged flux lower than that in the outburst phase. Moreover, other data sets in the radio, GeV, and TeV ranges considered in this Letter for multi-wavelength SED construction, are collected from long-term observations whereas the NuSTAR data for the XTE source are only observed during the outburst phase. Hence, to keep the multiwavelength SED-modeling consistent, we have assumed time-averaged X-ray fluxes from the XTE source. The assumed time-averaged X-ray fluxes used for model 1 and model 2 in

the 3–79 keV range are $F_X^{\mathrm{pl},1} \simeq (1.5 \pm 0.1) \times 10^{-13}$ erg cm^{-2} s^{-1} and $F_X^{\mathrm{pl},2} \simeq (4.4 \pm 0.3) \times 10^{-13}$ erg cm^{-2} s^{-1}, respectively. Although some uncertainties might be associated with the assumed X-ray flux values, the data are within the dynamic range of the XTE source, which future observations can verify.

Previously, Hinton et al. (2009), modeled the multiwavelength data of the TeV HMGB HESS J0632+057 using a one-zone leptonic model. We adopt the same value of the suppression factor due to the Klein–Nishina (KN) effect from Hinton et al. (2009), i.e., $f_{\mathrm{KN}}(E_e) \sim 10^{-3}$ for k$T_* \sim 3$ eV and $E_e = 1$ TeV. For this value of f_{KN}, the magnetic field was calculated from the relation $B \approx 5(f_{\mathrm{KN}}F_X/F_\gamma^{\mathrm{TeV}})^{0.5}$ G, where F_X and F_γ^{TeV} are fluxes of X-rays and TeV γ-rays (Abdalla et al. 2018a) respectively. We have considered a photon radiation density similar to that of Hinton et al. (2009), i.e., $U_{\mathrm{rad}} \sim 1$ erg cm^{-3}. The IC emission of ultrarelativistic electrons is happening in the deep KN regime (Hinton et al. 2009), as a result, the TeV γ-ray spectrum is softer compared to the X-ray spectrum produced by synchrotron emission. Such spectral variation was seen in X-ray and TeV ranges for our source (Halpern & Gotthelf 2007; Abdalla et al. 2018a), which is a characteristic feature of HMGBs.

We have studied the radiation from synchrotron and IC cooling of ultrarelativistic electrons, by solving the particle transport equation using publicly available code GAMERA[5] (Hahn 2015). We vary the total injected power in electrons, to fit the multiwavelength data of HESS J1828–099. The parameters required to explain the multiwavelength data in both cases are given in Table 2. Both model 1 and model 2, depicted in Figures 3(a) and (b) respectively, require a power of $\sim$(4–5) $\times 10^{35}$ erg s^{-1}. Although the multiwavelength one-zone models fail to reproduce the spectrum in the GeV range in both cases, the required luminosity in electrons of the models and the required parameters shown in Table 2 are consistent with those of the firmly established TeV HMGBs, thus indicating that HESS J1828–099 is possibly a TeV HMGB (Takata et al. 2017). We also present the cooling timescale and energy-loss rate of the IC and synchrotron mechanisms considered in our models, in Figures 3(c) and (d), respectively, for model 1 and in Figures 3(e) and (f), respectively, for model 2.

4. Discussion and Conclusion

The multiwavelength SED of HESS J1828–099 shown in Figure 3 closely resembles that of other known TeV HMGBs, as all of the firmly established HMGBs have hard X-ray spectra and significantly softer spectra in TeV energies. Through a detailed Fermi-LAT data analysis, the SED in the GeV energy range was also obtained. This type of spectral shape was seen previously in Tam et al. (2020), who assumed that GeV emission is due to some unrelated source such as supernova

---

[5] https://github.com/libgamera/GAMERA

remnant (SNR) G22.7–0.2, which is cospatial with HESS J1832–093 and 4FGL J1832.9–0913.

Because the resultant radiation from the hadronic p–p interaction between protons accelerated in the SNR shocks and cold protons clumped in nearby clouds can explain the analyzed GeV data, we have searched for SNRs in the vicinity of HESS J1828–099. SNR G021.5−00.1, which has been detected in radio observations, was thought to be spatially coincident with 4FGL J1830.2–1005 (Hewitt & Yusef-Zadeh 2009; Kilpatrick et al. 2015; Acero et al. 2016). Similarly, SNR G20.4+0.1, which is 1° away from HESS J1828–099, was assumed to be associated with the H.E.S.S. source (Abdalla et al. 2018b). However, it was found from THOR + VGPS data, as well as in GLIMPSE and WISE data, that these are clumped H II regions and not SNRs (Anderson et al. 2017). Recently, in the GLOSTAR Galactic plane survey data, four SNR candidates were identified: G021.492−0.010, G021.596−0.179, G021.684+0.129, and G021.861+0.169, which fall within the positional uncertainty of 4FGL J1830.2–1005 (Dokara et al. 2021); however, further observations are needed to establish a molecular cloud association with these SNRs. Alternatively, because 4FGL J1830.2–1005 is in a crowded region of the Galactic plane, contamination from nearby pulsars can be significant. We tried to find any bright GeV γ-ray emitting pulsar in the 4FGL catalog, in the nearby region of 4FGL J1830.2–1005, but did not find any. If future observations detect a pulsar in the vicinity of the 4FGL source that is contaminating the GeV emission, then it might be possible to explain the GeV data by gating off the pulsar contribution using up-to-date ephemeris. At present, studying these scenarios is beyond the scope of this work. Our model 2 also fails to explain the TGSS data at 147.5 MHz (see Figure 3(b)). Because the HMXBs show strong variability in the X-ray range and the TGSS radio measurements were performed at a different epoch than the X-ray observations, radio variability can be a possible reason behind this discrepancy. Alternatively, a completely different nonthermal low-energy radio component can also explain the TGSS data. Simultaneous observations in the X-ray and radio ranges can help address this discrepancy. While usually pulsars are the compact objects in HMGBs, such as PSR B1259–63 and PSR J2032+4127, there was a recent debate on the nature of the compact object in LS 5039, which may actually be a magnetar with a spin period of 9 s (Yoneda et al. 2020; Volkov et al. 2021; Yoneda et al. 2021). Although the spin period of the proposed magnetar is very close to the spin period of XTE J1829–098, the surface magnetic field of the magnetars is typically around 10^{13}–10^{15} G, whereas for the compact object in this binary source, the magnetic field is lower compared to that ($\approx 10^{12}$ G), confirming that the compact object in this HMXB system is indeed a pulsar and not a magnetar.

Based on the definition of HMGBs (Dubus 2006, 2013, 2015; Dubus et al. 2017), the emission typically dominates above 1 MeV. In the case of HESS J1828–099, the average GeV flux observed by Fermi-LAT, $F_\gamma^{\mathrm{GeV}} (\simeq (3.01 \pm 0.03) \times 10^{-11}$ erg cm^{-2} s^{-1}), is higher than the time-averaged X-ray flux values used both for model 1 and model 2, $F_X^{\mathrm{pl,1}}$ and $F_X^{\mathrm{pl,2}}$ respectively. Also from Figures 3(a) and (b), it can be seen that the multiwavelength SED peaks above 1 MeV. This nature of emission indicates that HESS J1828–099 can be classified as an HMGB. Furthermore, the required values of the parameters presented in Table 2 resemble those of known TeV HMGBs (Hinton et al. 2009; Skilton et al. 2009). We have kept the distance of the HMXB source (~10 kpc) fixed (Halpern & Gotthelf 2007). The environmental parameters such as

magnetic field (B) and radiation density (U_{rad}) were assumed according to Hinton et al. (2009), and they were also kept fixed. Age (t_{age}) and stellar photon temperature (T_*) were consistent with the Be companion star (Takata et al. 2017). The best-fit electron spectral index (α_e) was calculated considering the uncertainty in the power-law spectral index of the newly detected, subdominant, additional X-ray component produced in the shock region between the rotating pulsar magnetosphere and infalling stellar material. The magnetic fields used both for model 1 and model 2 are of the same order as in other established HMGBs (Hinton et al. 2009), indicating that our assumption of the time-averaged X-ray flux is reasonable. The electron injection luminosity is the only free parameter that was varied to fit the data. The minimum energy of the parent electron population E_{min} in model 1 is an upper limit, as the radio upper limits do not represent a detection themselves. Considering the offset between the Chandra position of XTE J1829–098 and the putative radio source, model 1 seems to be the favored interpretation of the source, although model 2 is also plausible. Taking into account the fact that this HMGB is at a larger distance compared to other known binaries, the required electron injection luminosity is consistent with that reported for other established HMGBs (Skilton et al. 2009; Eger et al. 2016; Takata et al. 2017).

In this Letter, we have performed GeV, X-ray, and radio data analyses and used results from previous infrared data analyses. From the X-ray data analysis, we have detected a subdominant hard X-ray tail in the NuSTAR source spectrum of XTE J1829–098, which suggests that the X-rays are produced via synchrotron cooling of shocked electrons. However, alternate interpretations for the hard X-ray tail include a compact jet, a hot corona, and an accretion disk, all of which have been observed in HMXBs (den Hartog et al. 2006; Wang et al. 2011). Long-term X-ray observations are necessary to confirm the origin of the hard X-ray emission. We have also performed one-zone modeling of the multiwavelength data of HESS J1828–099, and we have successfully reconciled radio, X-ray, and TeV data. Although our one-zone model strongly suggests that HESS J1828–099 is a TeV HMGB, the GeV data could not be explained by IC emission using this model. Emission from SNRs associated with molecular clouds and contamination from hitherto undetected nearby pulsars are some of the other possible scenarios that can explain the GeV emission. Nevertheless, based on positional coincidence and spectral information, as well as the agreeable fit of our one-zone model to the observed multiwavelength data and the consistency of the best-fit model parameters to those of previously studied HMGBs, we conclude that HESS J1828–099 is the TeV counterpart of the HMXB, thus contributing to the increasing number of TeV HMGBs detected. Further deep observations in different wavelengths and detailed modeling of the source are needed to confirm the nature of HESS J1828–099.

Appendix A
Monte Carlo Simulations

As pointed out in Protassov et al. (2002), the F-test in some cases does not (even asymptotically) adhere to their nominal χ^2 and F-distributions in many statistical tests common in astrophysics. Thus, in this case, the significance of the additional, subdominant power-law component depicting shock has been assessed through the Monte Carlo simulation method. The XSPEC tool `simftest` was used to perform this task. We used the model depicting the accretion component as our null hypothesis. The model, which includes the additional power-law component with the accretion component, was used as the alternate hypothesis. We simulated 1000 trials using `simftest` and calculated the change in χ^2 values for the null hypothesis and alternate hypothesis models. The maximum change in χ^2 ($\Delta\chi^2$) obtained from our simulations is 12.89. The probability of finding the observed change in χ^2 ($\Delta\chi^2_{obs} = 9.04$) by chance is 6×10^{-3}, which corresponds to 4σ significance. These results justify the addition of a subdominant power-law component, which in turn hints at the presence of shock in the source region of XTE J1829–098. The results of the simulations are reported in Figure 4.
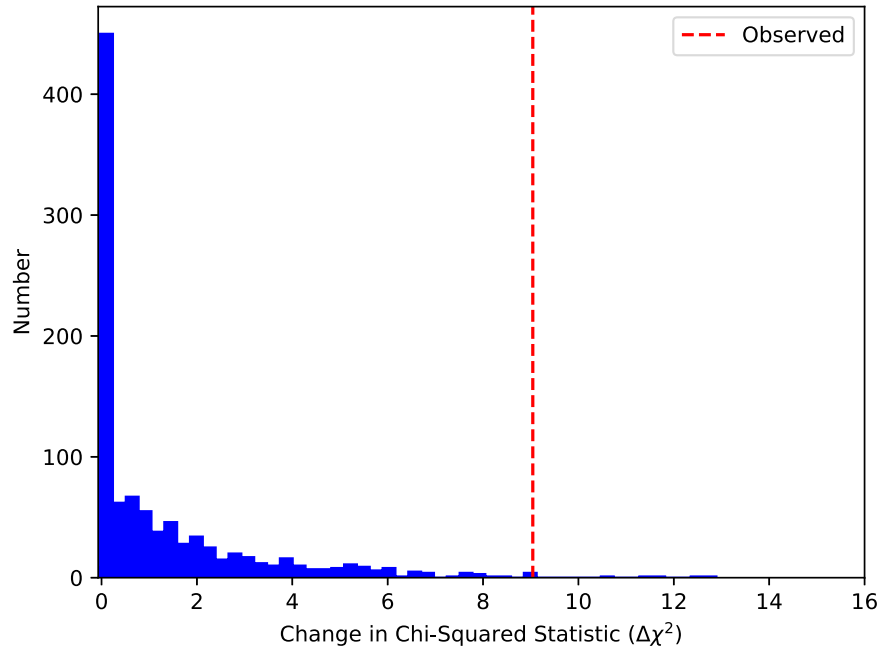
Figure 4. Results of 1000 Monte Carlo simulations to test the significance of the subdominant power-law component depicting shock. The blue solid histogram shows the frequency (*y*-axis) of $\Delta\chi^2$ values (*x*-axis) obtained in the simulations. The red dashed line shows the observed $\Delta\chi^2_{obs} = 9.04$.

Appendix B
Fermi-LAT Data Analysis

We have used Fermipy version 0.20.0[6] (Wood et al. 2017) to reduce and analyze ∼12 yr of PASS 8 LAT data in the energy range of 0.3–500 GeV. Events with zenith angles greater than 90° were excluded from the analysis to avoid contamination from Earth's albedo γ-rays. The instrument response function, Galactic diffuse emission template (galdiff), and isotropic diffuse emission template (isodiff) used in this work were "P8R3_SOURCE_V2", "gll_iem_v07.fits" and "iso_P8R3_SOURCE_V2_v1.txt," respectively. We have used the latest 4FGL catalog (Abdollahi et al. 2020) to search for the possible GeV counterpart of HESS J1828–099.

We have extracted the data from the Fermi-LAT website[7] considering a circular region of interest (ROI) having a radius of 10°, with the center of the ROI placed at the position of the H.E.S.S. source. Galdiff, isodiff, as well as all of the 4FGL sources within a rectangular region of 10° × 10°, centered on HESS J1828–099, were included in the analysis. Pulsar J1828–1007 is within 1° of the H.E.S.S. source, but it being a radio pulsar (Prinz & Becker 2015) does not affect our analysis. While analyzing the data, we have kept the parameters of all the 4FGL sources within 4° of the H.E.S.S. source free, including that of galdiff and isodiff. Using the source-finding algorithm of Fermipy, we also tried to find point sources around the H.E.S.S. source that are not included in the 4FGL catalog, having a minimum TS value of 25 and a minimum separation of 0°.3 between any two point sources. However, no plausible point sources in the GeV range were found in the vicinity of the H.E.S.S. source. All the best-fit values of the spatial and spectral parameters of the 4FGL sources, as well as galdiff and isodiff, were determined using maximum-likelihood analysis. Apart from the possible GeV counterpart 4FGL J1830.2–1005, the rest of the 4FGL sources, including galdiff and isodiff, were considered as background and subsequently subtracted during the analysis.

Appendix C
Periodicity Search

Because orbital periodicity is a distinguishable feature of HMGBs, in this work, we searched for periodicity in the ∼12 yr of Fermi-LAT γ-ray data observed from the source 4FGL J1830.2–1005. As discussed in Section 1, XTE J1829–098 has a possible orbital period of 246 days, as determined from the interval between consecutive outbursts. Because the 4FGL source is the possible GeV counterpart of the HMXB XTE J1829–098, we tried to find similar periodic variations in the light curve of the 4FGL source. To that end, we have produced light curves using the likelihood analysis for time bins of sizes ≈127 days, balancing low photon statistics and the idea to probe the periodicity of 246 days observed for the XTE source. The background model is considered to be the same as that used in Appendix B. No significant changes in the flux or spectral index were seen in different time bins. The 82.3 day and 177.7 day binned light curves were also produced, and again, no strong variability was found in either of the light curves, similar to the previous case.

Next, we searched for periodicity in the 127 day binned light curve, using a generalized Lomb–Scargle algorithm (Lomb 1976; Scargle 1982). The AstroML package (Vanderplas et al. 2012; Ivezić et al. 2014) was used to search for periodicity in the light curve between 1 and 300 days. We applied the bootstrapping statistical method to calculate the significance levels. Significance levels of 1% and 5% for the highest peak were calculated, determined by 10^5 bootstrap resamplings. No significant peak confirming any hint of periodicity was found in the generated power spectra. Bootstrapping indicates that no periodic signal was detected at 1% or 5% significance. The same method was reapplied for the 82.3 day and 177.7 day binned light curves, but even in those cases, no significant periodicity was detected. The nondetection of periodicity could be either due to inadequate statistics or due to a specific geometrical shape of the binary system that would not produce modulated emission in γ-rays (HESS Collaboration et al. 2015). This is similar to the case of the HMGB candidate HESS J1832–093, in which significant periodicity was also not confirmed (Tam et al. 2020). However, a detailed epoch-folding method (Martí-Devesa & Reimer 2020) can prove beneficial for finding any periodicity associated with 4FGL J1830.2–1005.

Appendix D
Radio Data Analysis

THOR provides the radio continuum image of ∼132 deg² of the Galactic plane observed with the Karl G. Jansky Very Large Array (VLA) in C-array configuration. Out of the eight SPWs covering 1–2 GHz, two are discarded due to excessive RFI. The other six SPWs (with 128 MHz bandwidth, centered at 1.06, 1.31, 1.44, 1.69, 1.82, and 1.95 GHz) are used to make the continuum images. Wang et al. (2020) used BLOBCAT (Hales et al. 2012) to identify sources and extract flux densities, as well as to estimate spectral index values from images at a common resolution of 25″. The rms noise values for individual SPW images are in the range 0.3–1.0 mJy beam⁻¹. All the images, flux density, and spectral index values are available publicly through the latest data release (Wang et al. 2020); we have used THOR individual SPW images and the combined THOR (VLA C array) and VGPS (VLA Galactic Plane Survey, which is the VLA D array and Effelsberg 100 m single-dish data combined; Stil et al. 2006) image to identify the potential counterpart and adopt the flux density values from the THOR catalog.

The C-band GLOSTAR survey, similarly, covers ∼145 deg² of the Galactic plane observed with the VLA B and D configurations along with the Effelsberg 100 m data to provide zero-spacing information. We use the GLOSTAR survey images from the VLA D configuration, with 18″ angular resolution and at an effective frequency of 5.8 GHz (shown in Figure 2). The continuum observations with the VLA were carried out using 16 SPWs with 128 MHz bandwidth each. The data are used to make eight continuum subimages covering 4.2–5.2 GHz and 6.4–7.4 GHz. We note that four radio sources are detected within the H.E.S.S. positional error in both THOR and the GLOSTAR surveys, but no X-ray counterparts are detected for any of these sources; so it is unlikely that these sources are associated with the H.E.S.S. source.

---

[6] https://fermipy.readthedocs.io/en/latest/
[7] https://fermi.gsfc.nasa.gov/ssc/data/access/lat/

ORCID iDs

Agnibha De Sarkar ● https://orcid.org/0000-0001-6047-6746
Nirupam Roy ● https://orcid.org/0000-0001-9829-7727
Pratik Majumdar ● https://orcid.org/0000-0002-5481-5040
Nayantara Gupta ● https://orcid.org/0000-0002-1188-7503
Andreas Brunthaler ● https://orcid.org/0000-0003-4468-761X
Karl M. Menten ● https://orcid.org/0000-0001-6459-0669
Sergio A. Dzib ● https://orcid.org/0000-0001-6010-6200
Sac Nicté X. Medina ● https://orcid.org/0000-0001-9536-7494
Friedrich Wyrowski ● https://orcid.org/0000-0003-4516-3981

References

Abdalla, H., Abramowski, A., Aharonian, F., et al. 2018a, A&A, 612, A1
Abdalla, H., Abramowski, A., Aharonian, F., et al. 2018b, A&A, 612, A3
Abdo, A. A., Ackermann, M., Ajello, M., et al. 2011, ApJL, 736, L11
Abdollahi, S., Acero, F., Ackermann, M., et al. 2020, ApJS, 247, 33
Abeysekara, A. U., Benbow, W., Bird, R., et al. 2018, ApJL, 867, L19
Acero, F., Ackermann, M., Ajello, M., et al. 2015, ApJS, 218, 23
Acero, F., Ackermann, M., Ajello, M., et al. 2016, ApJS, 224, 8
Ackermann, M., Ajello, M., Atwood, W. B., et al. 2016, ApJS, 222, 5
Aharonian, F., Akhperjanian, A. G., Aye, K. M., et al. 2005, A&A, 442, 1
An, H., Bellm, E., Bhalerao, V., et al. 2015, ApJ, 806, 166
Anderson, L. D., Wang, Y., Bihr, S., et al. 2017, A&A, 605, A58
Becker, P. A., Klochkov, D., Schönherr, G., et al. 2012, A&A, 544, A123
Bednarek, W. 2009, A&A, 495, 919
Ben Bekhti, N., Flöer, L., Keller, R., et al. 2016, A&A, 594, A116
Beuther, H., Bihr, S., Rugel, M., et al. 2016, A&A, 595, A32
Bogovalov, S. V., Khangulyan, D. V., Koldoba, A. V., Ustyugova, G. V., &
    Aharonian, F. A. 2008, MNRAS, 387, 63
Bosch-Ramon, V., & Paredes, J. M. 2004, A&A, 417, 1075
Bosch-Ramon, V., Barkov, M. V., Khangulyan, D., & Perucho, M. 2012,
    A&A, 544, A59
Brunthaler, A., Menten, K. M., Dzib, S. A., et al. 2021, A&A, 651, A85
Caliandro, G. A., Cheung, C. C., Li, J., et al. 2015, ApJ, 811, 68
Chakraborty, A., Roy, N., Wang, Y., et al. 2020, MNRAS, 492, 2236
Chang, Z., Zhang, S., Chen, Y.-P., et al. 2021, Univ, 7, 472
Chernyakova, M., Abdo, A. A., Neronov, A., et al. 2014, MNRAS, 439, 432
Condon, J. J., Cotton, W. D., Greisen, E. W., et al. 1998, AJ, 115, 1693
Corbet, R. H. D. 1984, A&A, 141, 91
Corbet, R. H. D. 1985, SSRv, 40, 409
Corbet, R. H. D. 1986, MNRAS, 220, 1047
Corbet, R. H. D., Chomiuk, L., Coe, M. J., et al. 2016, ApJ, 829, 105
Corbet, R. H. D., Chomiuk, L., Coe, M. J., et al. 2019, ApJ, 884, 93
den Hartog, P. R., Hermsen, W., Kuiper, L., et al. 2006, A&A, 451, 587
Dickey, J. M., & Lockman, F. J. 1990, ARA&A, 28, 215
Dokara, R., Brunthaler, A., Menten, K. M., et al. 2021, A&A, 651, A86
Dubus, G. 2006, A&A, 451, 9
Dubus, G. 2013, A&ARv, 21, 64
Dubus, G. 2015, CRPhy, 16, 661
Dubus, G., Guillard, N., Petrucci, P.-O., & Martin, P. 2017, A&A, 608, A59
Eger, P., Laffon, H., Bordas, P., et al. 2016, MNRAS, 457, 1753
Hahn, J. 2015, in Proc. of the International Cosmic Ray Conference
    (ICRC2015), 34 (Trieste: SISSA), 917
Hales, C. A., Murphy, T., Curran, J. R., et al. 2012, MNRAS, 425, 979
Halpern, J. P., & Gotthelf, E. V. 2007, ApJ, 669, 579
HESS Collaboration, Abramowski, A., Acero, F., et al. 2015, MNRAS,
    446, 1163

H.E.S.S. Collaboration, Abdalla, H., Abramowski, A., et al. 2018, A&A,
    610, L17
Hewitt, J. W., & Yusef-Zadeh, F. 2009, ApJL, 694, L16
Hinton, J. A., Skilton, J. L., Funk, S., et al. 2009, ApJL, 690, L101
Ho, W. C. G., Ng, C.-Y., Lyne, A. G., et al. 2016, MNRAS, 464, 1211
Huber, D., Kissmann, R., Reimer, A., & Reimer, O. 2021, A&A, 646, A91
Intema, H. T., Jagannathan, P., Mooley, K. P., & Frail, D. A. 2017, A&A,
    598, A78
Ivezić, Ž., Connolly, A., Vanderplas, J., & Gray, A. 2014, Statistics, Data
    Mining and Machine Learning in Astronomy (Princeton, NJ: Princeton
    Univ. Press)
Johnson, T. J., Wood, K. S., Kerr, M., et al. 2018, ApJ, 863, 27
Kalberla, P. M. W., Burton, W. B., Hartmann, D., et al. 2005, A&A, 440, 775
Karino, S., Nakamura, K., & Taani, A. 2019, PASJ, 71, 58
Kilpatrick, C. D., Bieging, J. H., & Rieke, G. H. 2015, ApJ, 816, 1
Lamb, F. K., Pethick, C. J., & Pines, D. 1973, ApJ, 184, 271
Li, J., Torres, D. F., Cheng, K.-S., et al. 2017, ApJ, 846, 169
Lomb, N. R. 1976, Ap&SS, 39, 447
Lovelace, R. V. E., Romanova, M. M., & Bisnovatyi-Kogan, G. S. 2005, ApJ,
    625, 957
Lyne, A. G., Stappers, B. W., Keith, M. J., et al. 2015, MNRAS, 451, 581
Maraschi, L., & Treves, A. 1981, MNRAS, 194, 1P
Markwardt, C. B., Halpern, J., & Swank, J. H. 2009, ATel, 2007, 1
Markwardt, C. B., Swank, J. H., & Smith, E. A. 2004, ATel, 317, 1
Martí-Devesa, G., & Reimer, O. 2020, A&A, 637, A23
Nakajima, M., Negoro, H., Kawamuro, T., et al. 2021, ATel, 14554, 1
Neronov, A., & Semikoz, D. V. 2010, arXiv:1011.0210
Prinz, T., & Becker, W. 2015, arXiv:1511.07713
Protassov, R., van Dyk, D. A., Connors, A., Kashyap, V. L., &
    Siemiginowska, A. 2002, ApJ, 571, 545
Reig, P. 2011, Ap&SS, 332, 1
Romanova, M. M., & Owocki, S. P. 2015, SSRv, 191, 339
Romero Torres, D. F., Kaufman Bernadó, M. M., Mirabel, I. F., et al. 2003,
    A&A, 410, L1
Scargle, J. D. 1982, ApJ, 263, 835
Sguera, V., Sidoli, L., Bird, A. J., Paizis, A., & Bazzano, A. 2019, MNRAS,
    491, 4543
Shtykovsky, A. E., Lutovinov, A. A., Tsygankov, S. S., & Molkov, S. V. 2018,
    MNRAS, 482, L14
Sironi, L., & Spitkovsky, A. 2011, ApJ, 741, 39
Skilton, J. L., Pandey-Pommier, M., Hinton, J. A., et al. 2009, MNRAS,
    399, 317
Stil, J. M., Taylor, A. R., Dickey, J. M., et al. 2006, AJ, 132, 1158
Takahashi, T., Kishishita, T., Uchiyama, Y., et al. 2009, ApJ,
    697, 592
Takata, J., Tam, P. H. T., Ng, C. W., et al. 2017, ApJ, 836, 241
Tam, P.-H. T., Lee, K. K., Cui, Y., et al. 2020, ApJ, 899, 75
Torres, D. F., Rea, N., Esposito, P., et al. 2012, ApJ, 744, 106
Vanderplas, J., Connolly, A., Ivezić, Ž., & Gray, A. 2012, in Conference on
    Intelligent Data Understanding (CIDU), 47
Verner, D. A., Ferland, G. J., Korista, K. T., & Yakovlev, D. G. 1996, ApJ,
    465, 487
Volkov, I., Kargaltsev, O., Younes, G., Hare, J., & Pavlov, G. 2021, ApJ,
    915, 61
Wang, J., Fabbiano, G., Risaliti, G., et al. 2011, ApJ, 729, 75
Wang, Y., Beuther, H., Rugel, M. R., et al. 2020, A&A, 634, A83
Wilms, J., Allen, A., & McCray, R. 2000, ApJ, 542, 914
Wood, M., Caputo, R., Charles, E., et al. 2017, in 35th International Cosmic
    Ray Conference (ICRC2017), 301 (Trieste: SISSA), 824
Yoneda, H., Khangulyan, D., Enoto, T., et al. 2021, ApJ, 917, 90
Yoneda, H., Makishima, K., Enoto, T., et al. 2020, PhRvL, 125, 111103